Design of a 3D-Printed Soft Robotic Hand with Integrated Distributed Tactile Sensing

Oliver Shorthose, Alessandro Albini, Liang He, and Perla Maiolino*

Abstract

Humans rely on distributed tactile sensing in their hands to achieve robust and dexterous manipulation of delicate objects. Soft robotic hands have received increased attention in recent years due to their adaptability to unknown objects and safe interactions with the environment. However, the integration of distributed sensing in soft robotic hands is lacking. This is largely due to the complexity in the integration of soft sensing solutions with the hands. This paper proposes a novel soft robotic hand that incorporates an active palm and distributed pneumatic tactile sensing in both the fingers and the palm. Multi-material 3D printing allows the tactile sensors to be directly printed on the hand, whereas conventional tactile approaches require the sensors to be attached as part of multiple fabrication procedures. Active degrees of freedom are introduced in the palm to achieve increased dexterity. The proposed hand successfully performed 32 of the 33 Feix taxonomy grasps and all 11 Kapandji thumb opposition poses.

Soft Robot Applications; Soft Sensors and Actuators; Multifingered Hands; Additive Manufacturing

1 Introduction

Research into soft robotics has increased over the last decade introducing soft, compliant materials to improve the safety and adaptability of robotic designs. The compliance allows for interaction with objects that vary in geometry and stiffness without requiring sophisticated control strategies. Specifically, robotic hands have received ample focus due to the interest in combining anthropomorphism with soft materials to achieve safe interaction and human-like dexterity [1–3].

Unlike many robotic hands that focus solely on finger and thumb actuation, humans use the degrees of freedom (DOFs) in the palm to achieve a wide range of grasp poses [4]. The adaptability of the human palm and the flexibility in creating contact configurations also increases the ability to ensure a robust grasp through uncertainty. This is compounded by the utilisation of passive

*

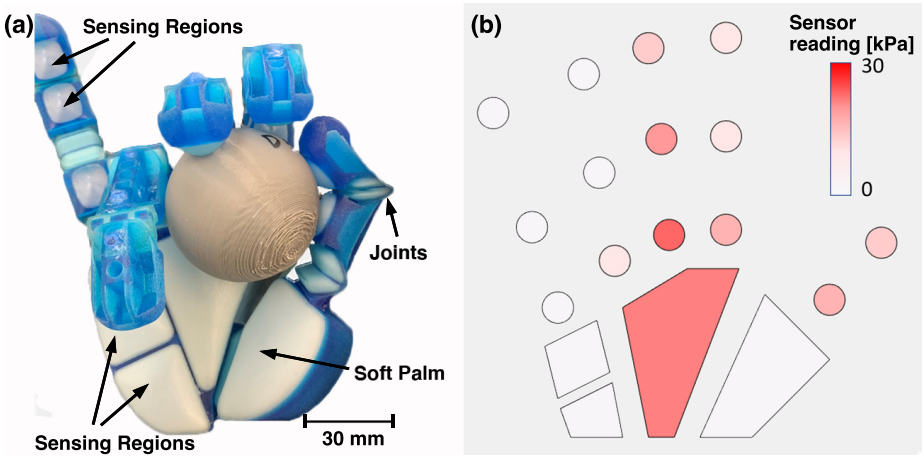

Figure 1: The proposed soft hand with the active palm and distributed tactile sensing. (a) The soft robotic hand grasping a sphere. The sensing regions and joints consist of 3D printed air chambers. (b) The corresponding sensor output from the distributed pneumatic sensing. In this visualisation, the color is related to the detected change in internal pressure.

compliance to interact with more diverse environments and establish greater dexterity [5]. Recently, soft robotic hand designs have been presented that incorporate active palms and passive compliance to improve their dexterity in manipulation [6–8]. Specifically, by mimicking the kinematics and softness of the human hand and implementing extra DOFs in the palm, soft robotic hands can interact with a wider variety of objects and achieve safer in-hand manipulation. For example, in [6], the authors proposed a 3 finger soft gripper with an active palm. The active palm allows the gripper to successfully grasp a wide variety of objects with different geometries and stiffnesses. Furthermore, the gripper compliance enables robust grasping with simple open-loop control. A soft humanoid hand with an active palm was proposed in [7]. The design demonstrated high compliance whilst grasping, thus avoiding damaging the grasped objects. Additionally, it was shown to be capable of performing a high number of different grasps from the Feix taxonomy [4]. In [8], the soft robotic hand design is inspired by a human hand model and it is composed of 26 independent DOF. The authors showed the possibility of achieving highly dexterous in-hand manipulation tasks. However, although the compliance of the hand has been successfully shown to be a key feature in achieving safe interaction with objects, these solutions lack a means of tactile sensing feedback to properly regulate the contact forces applied to the object and undertake precise in-hand manipulation [9–11]. Therefore, a lot of effort has been dedicated to the development of solutions providing soft robots with exteroceptive sensing [12].

In particular, tactile sensing has been shown to be essential in partnership with soft robotic hands or grippers to achieve safe and delicate object grasping

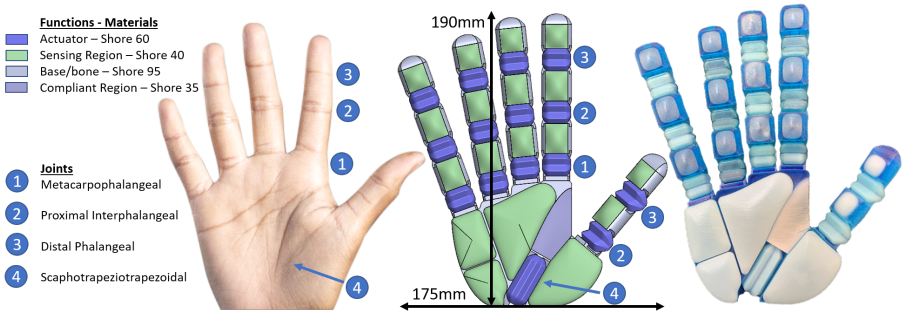

Figure 2: (Left): Human hand for scale and to indicate where each joint is; (Middle): CAD model of the soft robotic hand. The different regions are indicated in the legend with their respective Shore A hardness as follows: Blue, actuator, Shore A60; Green, sensing region, Shore A40; Grey, base/bones, Shore A95; Blue-grey, compliant region, Shore A35; (Right): The 3D printed hand. The total weight of the hand is 135g, the height is 190mm and the width is 175mm.

and manipulation [13–16].

For example, in [7] tactile sensors were integrated in the tips of a soft prosthetic hand enabling closed loop control of the grasping force. In [15] authors proposed a novel soft sensor that can be integrated on the tips of existing grippers to sense contact forces and the curvature of objects in their grasp. A monolithic soft robotic finger with an embedded tactile sensor in the tip was presented in [14]. In this solution, a soft pneumatic chamber was directly 3D-printed on the finger to detect tactile forces. The paper presented in [17] proposed a novel soft fingertip with embedded air cavities that can be used as a sensing element and actively change the shape of the fingertip, thus achieving a robust grasp while manipulating delicate objects. Although, these solutions have demonstrated the benefits of introducing tactile feedback to a soft gripper or finger, they allow to retrieve lumped contact information only. A more complete spatial information of the contact events can be attained from a distributed sensing network.

In particular, [18] provided distributed contact sensing capabilities on the fingers of a pneumatically actuated soft hand. An array of 4 flexible piezoresistive force sensors was integrated on each finger. The contact data were then used to train a neural network to classify a set of different grasping poses. Beyond the sensorisation of the fingers, [19] extended soft tactile sensing capabilities to the palm of a Shadow Hand (Shadow Robot Company, UK). Distributed contact sensing measurements were then exploited to classify objects' properties while performing in-hand manipulation. However, this integration cannot be easily performed on soft hands. Additionally, although [18] and [19] showed the advan-

tages of having a soft tactile sensing array in manipulation tasks, they still rely on an a posteriori integration procedure required to embed tactile sensors onto an existing hand. This can increase the risk of human error in the fabrication process or reduce the durability of the system.

The contribution of this paper is the novel design of a multi-material 3D printed soft robotic hand with an active palm, fully integrated with distributed tactile sensing capabilities. Fig. 1 shows the proposed hand. It contains 18 tactile sensing regions, consisting of 3D printed soft chambers. The soft pneumatic joints achieve controllable actuation for the active degrees of freedom. This is combined with passive compliance provided by the soft material to demonstrate successfully 32 out of the 33 required Feix taxonomy poses and all of the Kapandji opposition test poses. The designs proposed in [6–8] rely on silicone casting, thus requiring multi-step fabrication. Conversely, our design is monolithic and can therefore be fully 3D printed without requiring further integration of the parts, simplifying the fabrication of the hand. The solutions provided in [7, 14, 15, 17] have successfully integrated soft tactile sensors on robotic grippers or hands, however the sensing is limited to fingertips. Our design utilises distributed sensing to provide information over the contact locations and pressures applied on the hand. Additionally, by incorporating soft pneumatic pads, the design integrates an inherent compliance, allowing for greater adaptability to objects. The range of motion of each finger as well as the maximum grasping force have been characterised. Furthermore, the Feix Taxonomy and Kapandji Score [4, 20] have been evaluated to benchmark the dexterity of the whole hand.

The structure of the paper is as follows: Section 2 presents the design of the hand; Section 3 details the fabrication process; Section 4 reports the experiments performed to characterise the system; The result of the Feix Taxonomy and Kapandji Score are reported in Section 5; the Conclusion follows.

2 Hand Design and Actuation

The soft robotic hand is designed to attain dexterity comparable to a human hand in the fingers and palm. The hand incorporates the following design features: 1) soft actuation of the palm to increase the workspace of the thumb, 2) full coverage of the hand with soft pads to increase its adaptability and safety in grasping, 3) distributed sensing of the surface to provide tactile information of the object-hand interaction.

2.1 Palm and Hand Design

The geometry of the hand is designed based on human hand anatomy. The palm is introduced so that the soft thumb can reach the same places on the hand as a human thumb can, and the fingers have a comparable range of motion.

Similar to the human hand, the fingers are actuated at the metacarpophalangeal (MCP), proximal interphalangeal (PIP), and distal interphalangeal (DIP) joints, as shown by the actuator regions in Fig. 2. The desired bending range of

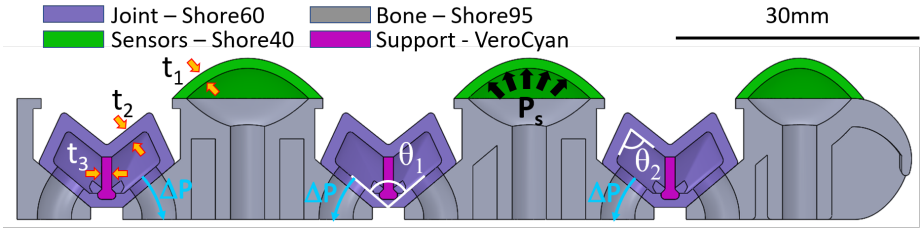

Figure 3: Cross-section of the finger. The different regions are indicated in the legend. P_s is the internal pressure on the soft pneumatic sensors and ΔP indicates the flow of air to evacuate the chambers. The dimensions are presented in mm: $t_1 = 1.25$; $t_2 = 1.5$; $t_3 = 1.0$; $\theta_1 = 100°$; $\theta_2 = 75°$.

each joint was determined by examining the mean value of the functional range of motion for the human finger joints [21]. This value was found to be 74°. To simplify the design process, this target was chosen to be identical for each joint.

The thumb was actuated at the scaphotrapeziotrapezoidal (STT), MCP, and interphalangeal (IP) joints. The desired bending angles were similarly deduced from a comparison to the human range of motion: STT abduction 42°; MCP flexion 53°; IP flexion 80° [22].

The positions of the MCP joints of each finger were determined from hand anatomy, taking the joint positions of an average human male [23]. Human fingers have a natural splay, with approximately 6° between the index and middle finger, 5° between middle and ring finger, and 10° between the ring and little finger. These angles were also incorporated into the design. To simplify the overall design, the fingers' joint lengths were constrained to be the same. The overall length of each finger was targeted at the average length of the average human male middle finger (93mm) [23].

Although the hand is soft, the integration of bone sections and compliant joints leads to a predictable motion of the hand that can be approximated as a set of joints, interconnected by rigid links. With the simplified kinematics, the angle of actuation between the base of the palm and the STT joint, and the axial rotation of the thumb are identified. The angle between the thumb and the base of the palm was determined to be 20°, and the axial rotation of the thumb is 30°. This configuration allows the thumb to come into contact with each fingertip, thereby demonstrating the design's dexterity.

2.2 Actuation

The fingers have three identical joints, the MCP, PIP and DIP, which can be independently actuated by applying negative pressure to each one of the M-shaped chambers (see Fig. 3). Vacuum actuation was chosen to achieve the required bending angle (74°) over a small region, which allows the kinematic simplification of discrete joints to be validated. Additionally, vacuum actuation was chosen over positive-pressure actuation to reduce the tensile stresses induced

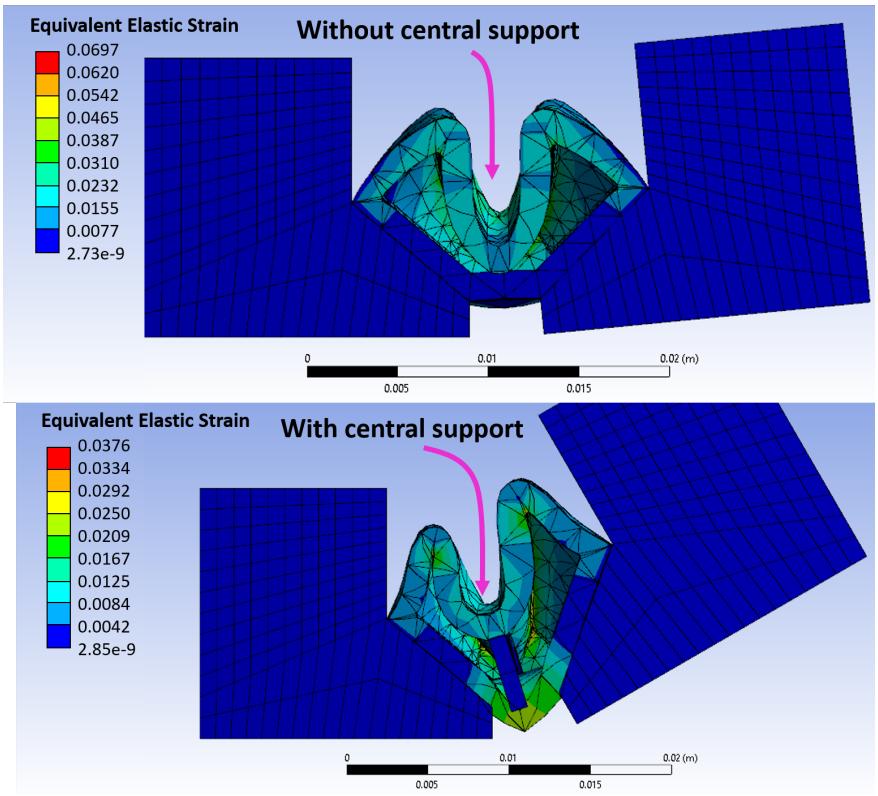

Figure 4: A comparison of the FEM study: (a) without the central support; (b) with the support. It can be noticed that rigid support in the centre prevents the chamber from collapsing in the undesired direction and supports the bending motion.

in the chambers [24].

Fig. 3 shows a cross-section through the finger, highlighting the different materials and geometries in the design. The design takes inspiration from an origami folding structure and uses a rigid centre support to prevent the chamber from collapsing [25]. The width and height of the fingers were chosen to fit roughly to the same size of a human finger (20mm).

The thumb and palm joints use the same M-shape design as the fingers. This simplifies the design process and reduces the necessary characterisation.

The fingers were simulated with Finite Element Modelling (FEM) in Ansys software (Ansys, Inc., USA) to validate geometry and design. Static structural tests were carried out using a Neo-Hookean hyperelastic model. The material properties of the Stratasys Digital Materials for the simulation were found in [26]. The shear modulus was computed as $G = \frac{E}{2(1+\nu)}$ where E is the Young's modulus and ν is the Poisson's ratio.

- To evaluate the material in the joints' performance under pressurisation, a negative pressure was applied to the interior surfaces whilst one of the bone pieces had a fixed boundary condition applied. The negative pressure was set at 10kPa as a mid-range target that would not cause material failure. The bending angle was taken as the angle between the two bone pieces either side of the joint and was compared between materials.

- To ensure the finger would not deflect under self-weight, gravity was applied over the body without any other external forces. The tip deflection was recorded for each joint material.

As a result of the simulations, Shore A60 Vero/Agilus blend was selected to fabricate the joints (tensile strength 3.5-4.5MPa, elongation at break 150-170%). Further details about the materials are also introduced in the Section III. Furthermore, the addition of the central support was simulated. Fig. 4 shows the simulated joint with and without the central support. Without the central support the joint flattened, not causing any bending motion, whereas the central support enforced a bending motion around the centre of the joint as desired.

2.3 Distributed Tactile Sensing

Pneumatic chambers are chosen as the tactile sensing methodology in the hand design due to the inherent sensor softness, and ease of integration with single-batch 3D printing [14, 17]. In this respect, the sensors are designed as air-filled soft membranes that are raised 4mm from the surface of the fingers and palm, with 1.5mm thickness and material stiffness of Shore A40 hardness. The pneumatic sensing units are distributed over the whole hand to capture the contact information of the entire surface area. The softness of the sensing skin provides additional adaptability and safety to the grasp.

In each finger, three soft sensing units cover the bone regions between each joint to ensure that the sensors are not affected as the finger bends (Fig. 3). In the palm, the regions were selected by assessing the most commonly used regions in the human hand for object manipulation [27]. The regions identified are the base of the thumb, and the region below the pinky finger, whereas the central region is used less frequently. The soft sensor above the STT joint is integrated as part of the active palm sensing region. In total, 18 independent sensing regions are introduced to the hand. The detailed distribution is shown in the green regions in Fig. 2.

3 Materials and Fabrication

The soft robotic hand is 3D printed using multi-material polyjet technology (J735, Stratasys Ltd, USA). This allows for monolithic integration of the soft sensing regions and the stiffer bone structures. For this design, a combination of Vero, a rigid plastic, and Agilus30, a rubber-like soft plastic was used [26].

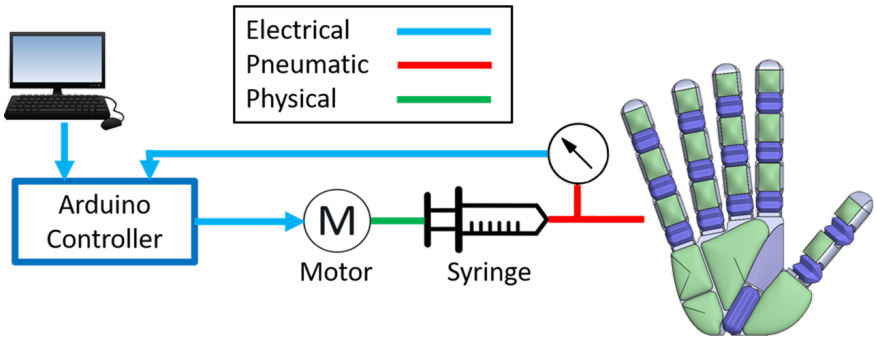

Figure 5: Control architecture for the soft hand. The Arduino controls the stepper motors, responding to real-time pressure values from the pressure sensors. The data from the Arduino and webcam is stored and post-processed to plot.

By changing the proportions of the two materials in a blend, the shore hardness of the material can be controlled (ShoreA [30,35,40,50,60,70,85,95]) [26].

The palm and thumb are printed monolithically, whilst the fingers are printed separately and attached via a simple slot connection. This allows for easy replacement of the fingers should they be damaged without having to reprint the entire hand. After printing, the support material is removed by placing the printed piece in a chemical bath (GEMINI SSR-550) filled with chemical support removal solution (0.02 kg/L Sodium Hydroxide and 0.01 kg/L Sodium Metasilicate).

The materials of each region are indicated in Fig. 2. The material of the joints was chosen to be Shore A60 after the simulation as detailed in Section 2. The main body was chosen to be Shore A95 to provide a small amount of compliance whilst providing sufficient strength to support the weight of the fingers and objects. The sensors are Shore A40 to allow for a greater degree of compliance whilst not failing under the applied load to compress the sensors.

4 System Characterisation

This section describes the experimental characterisation of the proposed design. In particular, we focused on the characterisation of 1) the range of motion of the fingers in relation to the pressure applied, 2) the output of the pressure sensors in relation to the applied force, 3) the overall grip strength of the hand where both the fingers and palm are involved in a grasping configuration.

4.1 Experimental Setup

A closed loop PID control executed on an Arduino board was used to set the desired pressure to actuate the joints. Each joint in the hand is connected using identical length tubes of 1mm internal diameter (ID) to a pressure sensor

(ADP5101) mounted on a PCB, remote from the hand, and connected to the Arduino board which samples the sensors' output at 50 Hz. The Arduino is also responsible for driving a set of stepper motors (Nema 17 Step with A4988 driver) actuating pneumatic syringes as depicted in Fig. 5. This sets the internal pressure of the joints as desired. The number of stepper motors and syringes required is dependant on the number of DOFs being controlled in any particular application.
The pneumatic chambers corresponding to tactile sensing elements were also connected via 1mm ID tubing to 18 different ADP51A11 pressure sensors and the measurements were sampled at 20 Hz using an Arduino.

4.2 Testing and Results

4.2.1 Range of motion

The fingers' range of motion was tested pseudo-statically by applying negative pressure to the chambers at 5kPa decrements until full actuation was achieved. The three joints in the finger were actuated concurrently. At each decrement, the pressure was held constant for 15 seconds to reduce any effect of hysteresis. The angle of the joints was recorded through a webcam using image acquisition software, *MATLAB image acquisition toolbox*, identifying markers at each joint and plotting the angle between them. Each characterisation test was repeated 5 times for 3 different printed models to test the repeatibility of the fabrication process. Between tests, the bodies were returned to a neutral position for 1 minute to allow any residual stresses to dissipate.

Fig. 6a displays the results of the fingers' range of motion. The average maximum bending angle of the individual joints was 70.0°. The average maximum angle between the first and last joints was 186.3°. The joints' output angles is slightly lower than the target angle of 74° discussed in Section 2. However, as shown in the next Section, this does not compromise the whole hand dexterity while performing the Feix and Kapandji tests.

A comparison of the simulated workspace against the real finger's workspace is presented in Fig. 6b. The simulated workspace is extrapolated from the kinematic simulation by examining the output position of the finger tip at each proposed output angle. Similarly, the real workspace is composed of the tip position at each angle recorded from the range of motion test. As shown, the workspaces have a considerable overlap, with a 2.7% difference in terms of areas between the simulated and real workspace.

4.2.2 Static sensor output

The output of the sensors, with respect to the force applied, was characterised by bringing a load cell into contact with the sensor and reading the pressure output. As shown in Fig.7, the load cell was connected to a flat plate that ensured the whole surface area was depressed. The load was held constant for 15 seconds to allow transient variations to dissipate. The force was increased

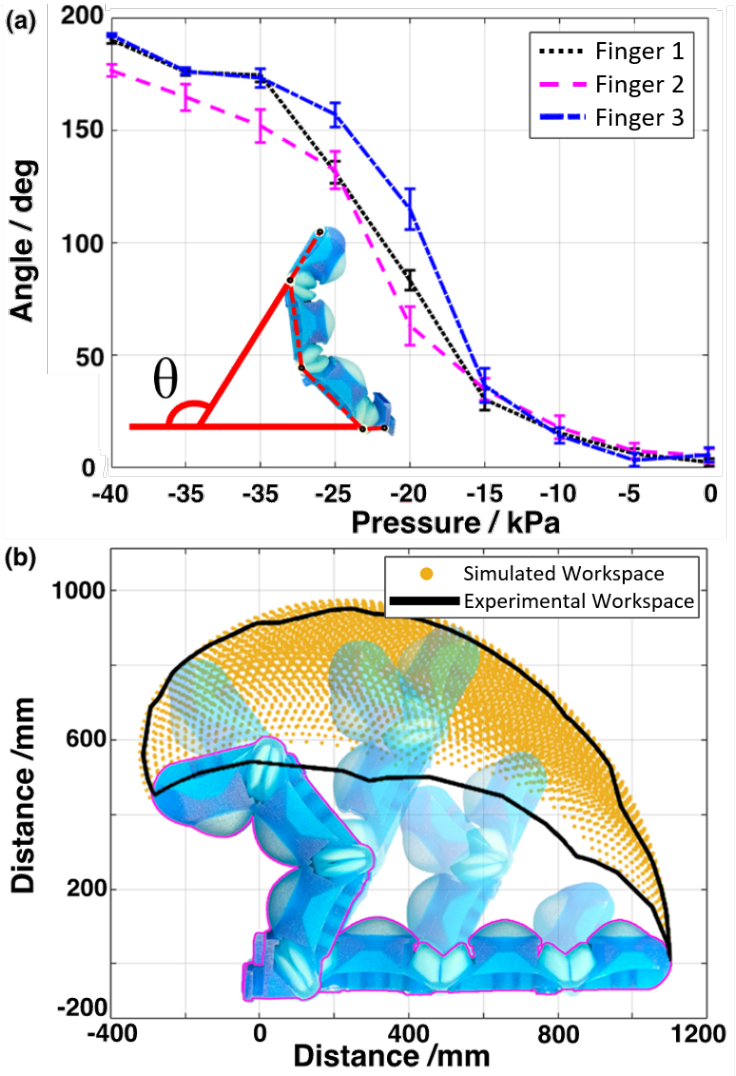

Figure 6: (a) Results of the range of motion tests for the fingers. The fingers were actuated in 5kPa decrementing pressure intervals and held for 15 seconds to ensure quasi-static conditions. The angle, θ presented is the angle between the first and last digits in the finger. (b) Range of motion for each finger. The yellow point cloud indicates the final position that the tip can reach depending on the application of pressure in each joint. The black line indicates the outline of the workspace that was observed experimentally.

by displacing the sensors further in 0.5mm increments and was removed from the sensor surface between increments. The load cell was mounted on a 3-axis

Shibaura BA-III cartesian robot. This procedure was repeated 6 times for each chamber on the fingers and three printed specimens were tested. The plot shown in Fig.7 shows the result of the characterisation. The mean standard deviation across the 30 experiments in the case of the pressure readings was 0.19kPa. The mean standard deviation for the force readings was 0.09N instead.

4.2.3 Dynamic sensor output

To test the sensors' dynamic response and durability, a 0.167Hz cyclic load was applied to the sensors with 0.5 second pause at the top and bottom of the stroke. The load was applied with the same flat plate used in the static sensor output test, mounted on the Shibaura BA-III cartesian robot. The plate depressed the sensor by 3mm repeatedly for 1,000 cycles. The small depression was chosen to ensure the material stayed within the linear elastic region. The sensitivity was analysed as the pressure delta over the force delta. The mean was found to be 2.31kPa/N; the standard deviation was 0.012kPa/N; the relative variation across the 1000 cycles was 1%.

4.2.4 Dynamic finger output

To test the fingers' response to cyclic actuation and durability, they were repeatedly actuated 500 times over 3 hours. A syringe was connected to a stepper motor and actuated to increase and decrease the volume of air in the joints by 10ml. The syringe paused for 7 seconds between tests to ensure the finger was static and residual stresses had subsided. The peak-to-peak pressure is analysed to assess whether any leakages developed or if the material had significantly softened. The mean peak-to-peak pressure was 54.85kPa, the standard deviation was 0.55kPa and the greatest difference between two cycles was 2.03kPa. 100 cycles have been isolated to show the detail of the test's results in Fig. 8.

4.2.5 Sensor hysteresis

To evaluate the amount of hysteresis exhibited by the pressure chambers, a 0.167Hz sinusoidal load was applied for 20 cycles. The hardware was the same as for the cyclic sensor output test and the sensor was similarly depressed by 3mm repeatedly but for 20 cycles. The result is displayed in Fig. 9. The maximum difference at a single applied force value was 3.82kPa, equating to 54% of the maximum recorded pressure.

4.2.6 Grip strength

The grip strength was characterised similarly to the work presented in [18]. In order to validate the combined strength of the fingers and palm, the hand's grip strength was tested by gripping a cylinder that was mounted to a load cell. In this test, the joints' chambers were connected to each other in the same actuation system (a single syringe as in Fig. 5). The hand was actuated by controlling the overall pressure to -35kPa in order to grasp the cylinder and

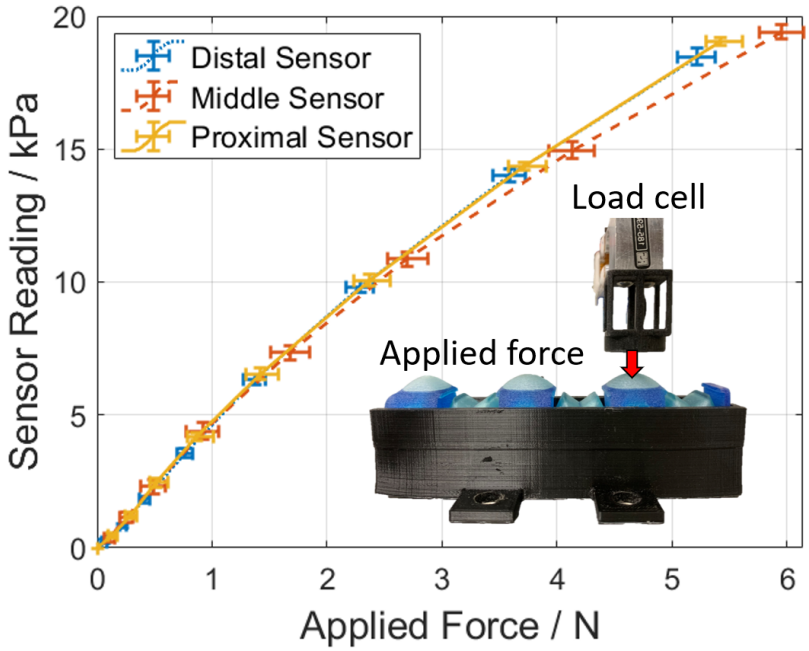

Figure 7: Results of the static sensor output test. A load cell was brought into contact with the three finger sensing chambers and held statically for 15 seconds before being removed between tests. The displacement was increased by 0.5mm between tests. Each data point indicates the values read at the 0.5mm increments.

to test the maximum grip strength. The cylinder was then raised at 5mm/sec until the grasp slipped and the force was reduced. The output of the load cell was recorded throughout and Fig. 10 shows the physical setup for this test. This procedure was repeated 6 times. The load cell is connected to a Shibaura BA-III cartesian which ensures a steady vertical motion. The results of the grip strength test are shown in Fig. 10 with the profile indicating how the force in the load cell varies as the grasping frame is raised. The peak indicates the mean maximum grip force among all the 6 experiments, which was found to be 6.42N with a standard deviation of 0.29N.

5 Hand Dexterity Validation

5.1 Feix Taxonomy

The goal of this Section is to validate the kinematic of the hand and its passive compliance by evaluating its performance on the Feix taxonomy poses and the Kapandji opposition test poses.

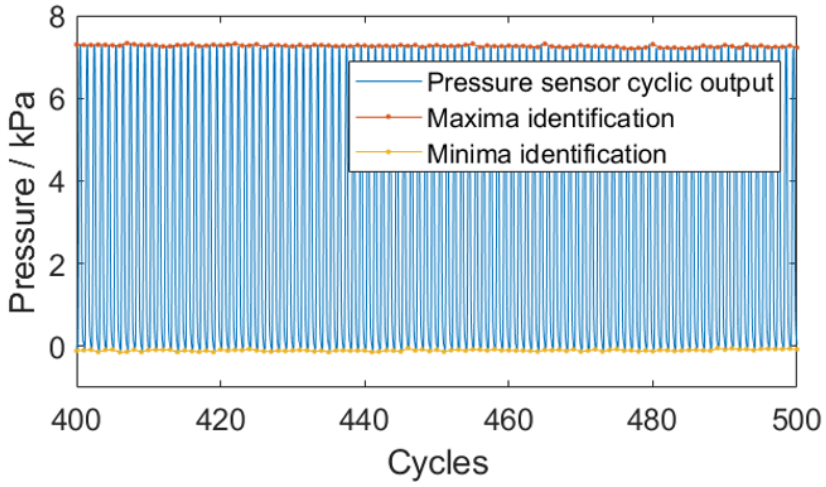

Figure 8: Results of the dynamic sensor output test. A load cell was cyclically brought into contact with the three finger sensing chambers at 0.167Hz. A pause of 0.5 seconds was introduced at the top and bottom of each stroke. The maxima and minima are highlighted

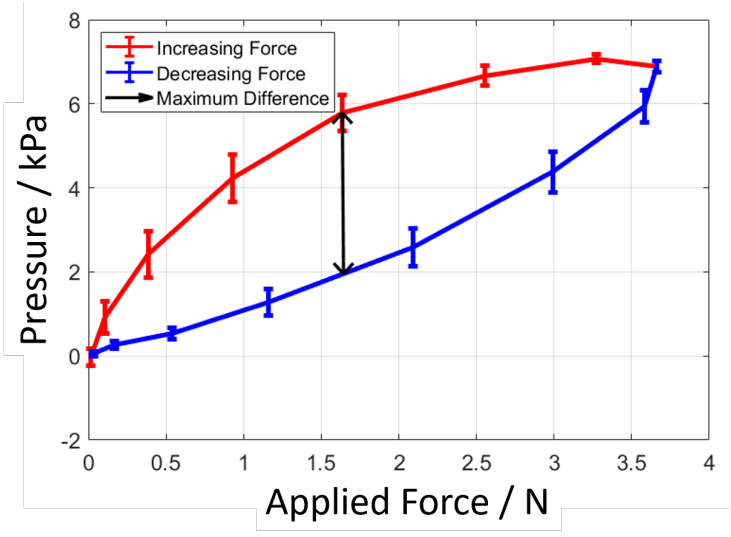

Figure 9: Results of hysteresis cyclic test. The load cell was depressed and released by 3mm repeatedly at 0.167Hz for 20 cycles. The lines show the mean of the increasing and decreasing cycles respectively with the point of maximum difference highlighted.

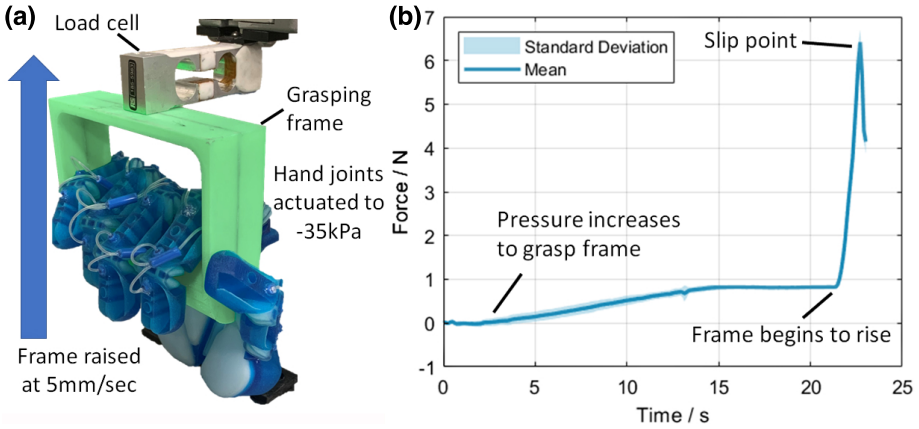

Figure 10: Results of the grasp strength tests. (a) Physical setup for the grasp strength test. The frame and load cell are connected to a Shibaura BA-III Cartesian robot. (b) Graph of the grasp strength test's results. The pressure was decreased to -35kPa as the hand came into contact with the frame. The frame was then raised at 5mm/sec until the the grasp slipped.

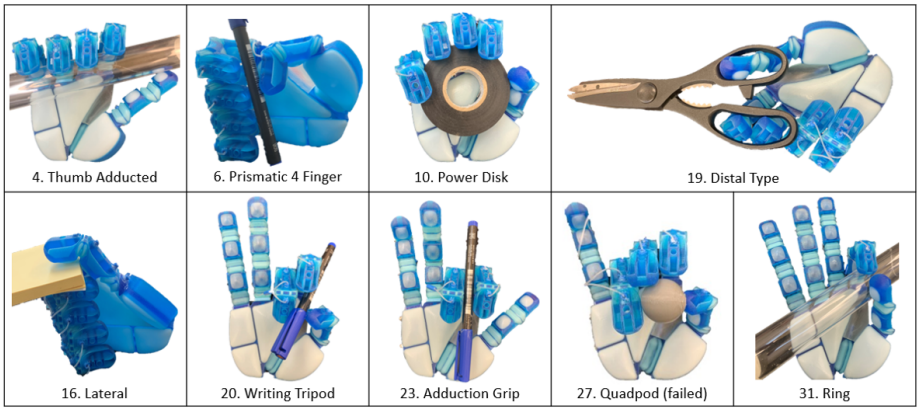

Figure 11: A selection of the 33 completed grasps from the Feix taxonomy tests used as a dexterity benchmark. Each pose was held for 30 seconds to verify stability. These poses have been selected for presentation as they demonstrate the widest range of grasps in the taxonomy.

The Feix taxonomy is a set of 33 grasp poses that aims to encompass the dexterity of the human hand. The tests were undertaken by analysing the relevant DOFs to actuate, the amount of actuation for each DOF, and the objects required to validate the grasp. The object was then placed in the hand and grasped for 30 seconds to ensure stability was achieved. The hand successfully

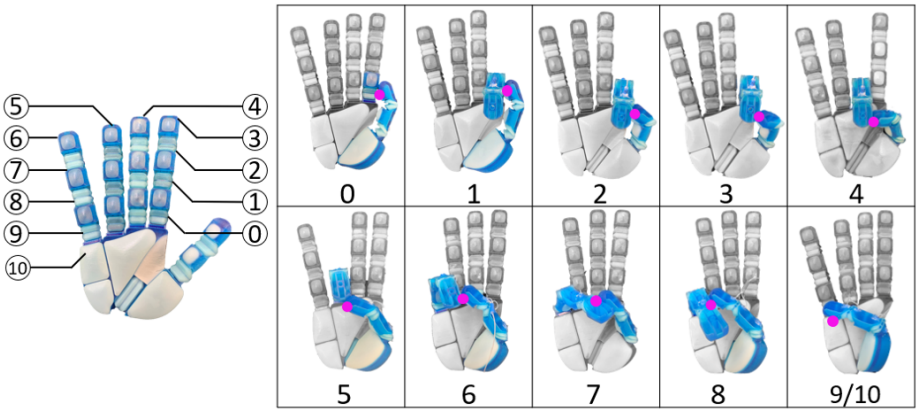

Figure 12: Results of the Kapandji tests. The thumb was brought into contact with each assigned position on the hand in accordance with the Kapandji thumb opposition test. Each position was held for 30 seconds. The magenta dots indicate the points of contact between the thumb and rest of the hand. The colored regions show the DOFs that are active in each pose.

displayed 32 of the 33 grasps, with pose 27, the quadpod, being unsuccessful (see Fig. 11). The pose was categorised as a failure because it could not entirely grasp at the finger tip pads and required the side of the distal joint of the fourth finger to support the object. In future designs of the hand, this failure will be addressed by adding controlled splay to the fingers by increasing the number of DOFs in the MCP of the fingers.
Fig. 11 shows a selection of the grasps that demonstrate: precision grasps (6, 19 and 20), power grasps (4, 10 and 31), a side grasp (16) and the use of passive compliance to achieve a grasp (23). The full list of images representing all the 33 grasps configuration can be found in the attached video, provided as a supplementary material.

5.2 Kapandji test

The Kapandji test originates from assessing a patients thumb opposition and ability to reach different regions of the hand and fingers. There are 11 points that need to be reached to achieve the full score. As with the Feix tests, the relevant DOFs were actuated until the desired points were brought into contact. The position was then maintained for 30 seconds to validate controlled motion.

The hand achieved all 11 of the opposition poses. Therefore, this experiment validates the human-like dexterity of the soft hand. The results are presented in Fig. 12 and demonstrate that the thumb opposition is similar to a human hand.

6 Conclusion

In this paper, we have presented the design of an anthropomorphic soft robotic hand with distributed tactile sensing. The hand is 3D printed using polyjet technology to simplify the manufacturing process and allow for monolithic multi-material integration. The tactile sensors are designed as compliant pneumatic chambers embedded into the surface.

The finger joints' were characterised and display an average maximum output angle of 70° per joint. The workspace of the fingers is presented with close similarity to a simulated workspace based on a human finger's range of motion.

The whole hand was characterised with a grasping strength test, the Feix Taxonomy test, and the Kapandji Score test. The maximum grasping force was found to be 6.42N and the hand could achieve 32 of the 33 requisite poses for the Feix test and all of the poses in the Kapandji test.

In future iterations of the hand, the failed Feix taxonomy pose will be addressed by considering the splaying motion of the hand as an extra DOF.

As shown in Fig 1 the distributed tactile sensing system allows for the monitoring of contact pressures applied by the hand during the interaction with objects. This opens the possibility for further extension of the work exploiting closed loop control algorithms to achieve dexterous in-hand manipulation and fine control of the contact forces. A simple demonstration of the response of the tactile system is included in the video provided as supplementary material.

References

[1] J. Hughes, U. Culha, F. Giardina, F. Guenther, A. Rosendo, and F. Iida, "Soft manipulators and grippers: A review," p. 1, nov 2016. [Online]. Available: www.frontiersin.org

[2] C. Piazza, G. Grioli, M. G. Catalano, and A. Bicchi, "A Century of Robotic Hands," *Robotics, and Autonomous Systems Annu. Rev. Control Robot. Auton. Syst. 2019*, vol. 22, pp. 1–32, 2019.

[3] Z. Wang, T. Hirata, T. Sato, T. Mori, M. Kawakami, H. Furukawa, and S. Kawamura, "A Soft Robotic Hand Based on Bellows Actuators for Dishwashing Automation," *IEEE Robotics and Automation Letters*, vol. 6, no. 2, pp. 2139–2146, 2021.

[4] T. Feix, J. Romero, H. B. Schmiedmayer, A. M. Dollar, and D. Kragic, "The GRASP Taxonomy of Human Grasp Types," *IEEE Transactions on Human-Machine Systems*, vol. 46, no. 1, pp. 66–77, 2016.

[5] J. A. Hughes, P. Maiolino, and F. Iida, "An anthropomorphic soft skeleton hand exploiting conditional models for piano playing," *Science Robotics*, vol. 3, no. 25, pp. 1–13, 2018.

[6] V. Subramaniam, S. Jain, J. Agarwal, and P. Valdivia y Alvarado, "Design and characterization of a hybrid soft gripper with active palm pose control," *The International Journal of Robotics Research*, vol. 39, no. 14, pp. 1668–1685, dec 2020.

[7] H. Wang, F. J. Abu-Dakka, T. N. Le, V. Kyrki, and H. Xu, "A novel design of soft robotic hand with a human-inspired soft palm for dexterous grasping," *arXiv*, pp. 1–9, 2020.

[8] J. Zhou, X. Chen, U. Chang, J. T. Lu, C. C. Y. Leung, Y. Chen, Y. Hu, and Z. Wang, "A soft-robotic approach to anthropomorphic robotic hand dexterity," *IEEE Access*, vol. 7, pp. 101 483–101 495, 2019.

[9] Q. Lu, L. He, T. Nanayakkara, and N. Rojas, "Precise in-hand manipulation of soft objects using soft fingertips with tactile sensing and active deformation," in *2020 3rd IEEE International Conference on Soft Robotics (RoboSoft)*, 2020, pp. 52–57.

[10] L. He, Q. Lu, S.-A. Abad, N. Rojas, and T. Nanayakkara, "Soft fingertips with tactile sensing and active deformation for robust grasping of delicate objects," *IEEE Robotics and Automation Letters*, vol. 5, no. 2, pp. 2714–2721, 2020.

[11] S. E. Navarro, S. Nagels, H. Alagi, L.-M. Faller, O. Goury, T. Morales-Bieze, H. Zangl, B. Hein, R. Ramakers, W. Deferme, G. Zheng, and C. Duriez, "A model-based sensor fusion approach for force and shape estimation in soft robotics," *IEEE Robotics and Automation Letters*, vol. 5, no. 4, pp. 5621–5628, 2020.

[12] H. Wang, M. Totaro, and L. Beccai, "Toward Perceptive Soft Robots: Progress and Challenges," sep 2018. [Online]. Available: https://onlinelibrary.wiley.com/doi/full/10.1002/advs.201800541

[13] G. Gu, N. Zhang, H. Xu, S. Lin, Y. Yu, G. Chai, L. Ge, H. Yang, Q. Shao, X. Sheng, X. Zhu, and X. Zhao, "A soft neuroprosthetic hand providing simultaneous myoelectric control and tactile feedback," *Nature Biomedical Engineering*, 2021. [Online]. Available: http://dx.doi.org/10.1038/s41551-021-00767-0

[14] C. Tawk, H. Zhou, E. Sariyildiz, M. In Het Panhuis, G. Spinks, and G. Alici, "Design, Modeling and Control of a 3D Printed Monolithic Soft Robotic Finger with Embedded Pneumatic Sensing Chambers," *IEEE/ASME Transactions on Mechatronics*, vol. 4435, no. c, pp. 1–1, jul 2020.

[15] H. Yang, Y. Chen, Y. Sun, and L. Hao, "A novel pneumatic soft sensor for measuring contact force and curvature of a soft gripper," *Sensors and Actuators, A: Physical*, vol. 266, pp. 318–327, 2017. [Online]. Available: http://dx.doi.org/10.1016/j.sna.2017.09.040

[16] Q. Lu, L. He, T. Nanayakkara, and N. Rojas, "Precise in-hand manipulation of soft objects using soft fingertips with tactile sensing and active deformation," in *2020 3rd IEEE International Conference on Soft Robotics (RoboSoft)*, 2020, pp. 52–57.

[17] L. He, Q. Lu, S. A. Abad, N. Rojas, and T. Nanayakkara, "Soft Fingertips with Tactile Sensing and Active Deformation for Robust Grasping of Delicate Objects," *IEEE Robotics and Automation Letters*, vol. 5, no. 2, pp. 2714–2721, 2020.

[18] P. M. Khin, J. H. Low, M. H. Ang, and C. H. Yeow, "Development and Grasp Stability Estimation of Sensorized Soft Robotic Hand," *Frontiers in Robotics and AI*, vol. 8, mar 2021. [Online]. Available: https://www.frontiersin.org/articles/10.3389/frobt.2021.619390/full

[19] G. Buscher, M. Meier, G. Walck, R. Haschke, and H. J. Ritter, "Augmenting curved robot surfaces with soft tactile skin," *IEEE International Conference on Intelligent Robots and Systems*, vol. 2015-Decem, pp. 1514–1519, 2015.

[20] A. Kapandji, "Cotation clinique de l'opposition et de la contre-opposition du pouce," *Annales de Chirurgie de la Main*, vol. 5, no. 1, pp. 67–73, jan 1986.

[21] G. I. Bain, N. Polites, B. G. Higgs, R. J. Heptinstall, and A. M. McGrath, "The functional range of motion of the finger joints," *Journal of Hand Surgery: European Volume*, vol. 40, no. 4, pp. 406–411, 2015.

[22] P. Levangie and C. Norkin, *Joint Structure and Function: A Comprehensive Analysis*, 5th ed. F.A. Davis, 2011. [Online]. Available: https://www.amazon.co.uk/Joint-Structure-Function-Comprehensive-Analysis/dp/0803623623

[23] A. Buryanov and V. Kotiuk, "Proportions of Hand Segments," *International Journal of Morphology*, vol. 28, no. 3, pp. 755–758, 2010.

[24] C. Tawk, G. M. Spinks, M. In Het Panhuis, and G. Alici, "3D Printable Linear Soft Vacuum Actuators: Their Modeling, Performance Quantification and Application in Soft Robotic Systems," *IEEE/ASME Transactions on Mechatronics*, vol. 24, no. 5, pp. 2118–2129, 2019.

[25] J.-g. Lee and H. Rodrigue, "Origami-Based Vacuum Pneumatic Artificial Muscles with Large Contraction Ratios," *Soft Robotics*, vol. 6, no. 1, 2019.

[26] *Digital Materials Data Sheet*, Stratasys, 2020. [Online]. Available: https://www.stratasys.com/-/media/files/material-spec-sheets/mss_pj_digitalmaterialsdatasheet_0617a.pdf

[27] S. Sundaram, P. Kellnhofer, Y. Li, J.-Y. Zhu, A. Torralba, and W. Matusik, "Learning the signatures of the human grasp using a scalable tactile glove," *Nature*, vol. 569, no. 7758, pp. 698–702, may 2019. [Online]. Available: https://doi.org/10.1038/s41586-019-1234-zhttp://www.nature.com/articles/s41586-019-1234-z